Resonance Principle for the Design of Flapping Wing Micro Air Vehicles

Jian Zhang and Xinyan Deng, *Member, IEEE*

Abstract—Achieving resonance in flapping wings has been recognized as one of the most important principles to enhance power efficiency, lift generation, and flight control performance of high-frequency flapping wing micro air vehicles (MAVs). Most work on the development of such vehicles have attempted to achieve wing flapping resonance. However, the theoretical understanding of its effects on the response and energetics of flapping motion has lagged behind, leading to suboptimal design decisions and misinterpretations of experimental results. In this work, we systematically model the dynamics of flapping wing as a forced nonlinear resonant system, using both nonlinear perturbation method and linear approximation approach. We derived an analytic solution for steady-state flapping amplitude, energetics, and characteristic frequencies including natural frequency, damped natural frequency, and peak frequency. Our results showed that both aerodynamic lift and power efficiency are maximized by driving the wing at natural frequency, instead of other frequencies. Interestingly, the flapping velocity is maximized at natural frequency as well, which can lead to an easy experimental approach to identify natural frequency and validate the resonance design. Our models and analysis were validated with both simulations and experiments on ten different wings mounted a direct-motor-drive flapping wing MAV. The result can serve as a systematic design principle and guidance in the interpretations of empirical results.

Index Terms—Aerial robotics, biologically inspired robotics, flapping flight, microrobotics, resonance.

I. INTRODUCTION

SIGNIFICANT progress has been made in the understanding of the exceptional flight stability and agility of insects and hummingbirds with flapping wings [1]–[3]. Flapping wing can generate elaborate wing motion therefore produce rapidly changing instantaneous aerodynamic forces and torques with minimum actuation. This ability makes it an attractive alternative to conventional micro air vehicles (MAVs) with rotary wing-based solutions and inspires the development of flapping wing MAVs. Actuating the reciprocal flapping wing motion involves rapid acceleration and deceleration during stroke reversals and, therefore, can be quite power intensive. Power is consumed in overcoming not only the aerodynamic drag, but also the substantial wing inertia due to constantly oscillating wings and accompanying mechanisms that move at high frequency [4]. Therefore, mechanical resonance has been recognized as one of the key principles for reducing wing actuation complexity and power consumption. In the ideal scenario, with elastic components and system operating at resonance, the kinetic and potential energy of the moving components would be conserved, and therefore, power is spent only on the nonconservative energy cost, such as friction and the aerodynamic damping from the wing.

Biological evidence such as that in [17] and [18] speculated the flapping wing as an oscillator. Based solely on large amount of observation of different species, Greenewalt [17] speculated that the muscular energy should be at the minimum when the muscular driving force is in resonance with the system. A more recent study of Dudley [18] showed that the wingbeat frequency of individual insects is fairly constant with the variation within 5% in typical hovering flight. They hypothesized that at this relative constant frequency, which may be the resonant frequency of oscillation, the energetic expenditure is minimized. Furthermore, by experimental perturbation of wing inertia, they showed predicted changes in resonant frequency. The direct implementation of resonant oscillation on flapping wing MAV, however, is complicated due to the lack of a comprehensive understanding of the wing-thorax system including the unsteady time-varying aerodynamics, complex fluid-structure interactions, and nonlinear linkage transmission.

Despite the lack of theoretical guidance and the difficulty in resonance tuning, the past several years have seen numerous advances in designing and prototyping high-frequency flapping wing actuation and mechanisms across different scales. At subgram scale, in order to reduce the required power for flapping motion, the piezoelectric (PZT) bending cantilever has been developed to resonate with actuator's material property [6], [7], [19]. With this design, the Harvard's insect-size robot has demonstrated lifting off [6] and controlled flight [20]. Meanwhile, at grams to tens-of-grams scale, motor-driven thorax-wing systems were successfully developed, operating at low input voltage with higher payload. This form of actuation can be further divided into linkage mechanisms and direct-drive types. Linkage mechanisms transfer rotational motion from the motor to reciprocal motion of the wings through four-bar or equivalent four-bar mechanisms. Several works added elastic elements to improve the four-bar linkage mechanism that resulted in limited success [21]–[25], largely due to the fact that the highly

nonlinear and asymmetric linkage transmissions hinder the full recovery of potential energy from sinusoidal wing motion. Recently, direct-drive type is gaining popularity with works such as [11], [14], [26], where each flapping wing is driven directly using a geared DC motor without linkages, while the motor undergoes reciprocating rotation. Prototypes that achieved liftoff was demonstrated in [14].

The widely adopted method to identify and validate the resonance of the system is by conducting a frequency sweep, during which the wing is driven by sinusoidal voltage inputs with a wide range of frequencies of interest [6], [14]. The steady-state amplitudes of the responses in terms of flapping angles would then be plotted with respect to input frequencies. Other interested output such as the steady-state velocities of the responses or stroke-averaged lifts can also be plotted similarly. A typical second-order resonant system can be characterized by natural frequency, damped natural frequency, and peak frequency. Natural frequency is also called the primary resonant frequency and is a function of system inertia and stiffness. Damped natural frequency is the frequency of free response of a linear second-order systems. For linear underdamped second-order systems, peak frequency is also called peak resonance frequency or resonant frequency, corresponding to the maximum amplitude (flapping angle for example) from frequency response. The term resonant frequency has often been loosely used to indicate the peak frequency. Moreover, it is also defined to be the natural frequency in the context of nonlinear vibration. To avoid the misinterpretation of resonance frequency, here, we use natural frequency and peak frequency instead. Only when the system damping is sufficiently small, these three frequencies converge close to one other in their values. As shown in many previous works and this study, flapping wing typically is underdamped, although it has sufficiently large damping from aerodynamics. So we will show that the penalties of using the wrong frequency cannot be ignored.

Due to its simplicity, a linear model with passive rotation and quasi-steady aerodynamic model was adopted in previous work to model flapping wing. For PZT bending cantilever beam actuation mechanisms [27], the nonlinear aerodynamic damping was linearized about mid-stroke with maximum drag, giving a "worst-case" estimate for aerodynamic damping. In [14], Hines *et al.* assumed zero rotational angles for the nonlinear aerodynamic damping. Those simplifications could lead to discrepancies on the evaluation of aerodynamic damping effects. In this work, we will show the limitations of linear model and complement it with nonlinear modeling and analysis in order to gain a full picture of the system response at different frequencies around resonance.

Flapping wing resonance tuning, however, still suffers from suboptimal design decisions and misinterpretations of experimental results, owing to the lack of theoretical analysis of resonance's effect on the response and energetics of flapping wing. Currently, most work in this area still relies heavily on empirical testings. The authors of [6], [11], [16], and [28] have optimized the flapping amplitude. While this is believed to yield maximum rotation angles, this does not necessarily optimize lift and efficiency, as suggested by our theoretical analysis and experiments.

While work such as [29], [30] where the wing was driven at damped natural frequency with a goal to achieve optimal efficiency, other work measured peak frequency from the frequency response experiments to validate the calculation of the natural frequency [26], [28], [31]. In [14], the peak frequency was used as the indication of maximum lift and optimal efficiency, while in the frequency response experiment, it was observed that the peak frequency was actually lower than the one, under which maximum lift was produced (off-resonance maximum lift). Similar results were also found in [28] and [31]. In fact, here, we will show that maximum lift is produced at natural frequency, which is normally higher than the peak frequency, thus explaining the observed discrepancies.

In addition, for most of the previous works, the flapping resonance was designed as an independent variable, thereby requiring a large number of tests to characterize and verify choice of system parameters and yielding little insight for the overall systematic design.

In this work, we present a theoretical analysis of flapping resonance, focusing on its effects on steady-state response, lift generation, and energetics. A simplified dynamic model for the thorax-wing system was used to model it as a forced resonance of a nonlinear second-order system. The dynamic model was analyzed with the nonlinear perturbation method. We obtained the closed-form solutions of steady-state system response and averaged power as a function of system parameters at natural frequency. The nonlinear dynamic model was then approximated with a linear model, in which we derived analytic formulas to predict the steady-state responses and three characteristic frequencies including natural frequency, damped natural frequency, and peak frequency. Our analysis revealed the following.

1) The peak value of flapping angle velocity occurs when driving the system at natural frequency.
2) The maximum lift occurs at natural frequency, not peak frequency.
3) The maximum efficiency is achieved at natural frequency, not the peak frequency.

The model and analysis were validated with simulations and experiments on ten wings mounted on a direct-motor-drive MAV.

The rest of this paper is organized as follows. Section II presents the modeling of the wing. Section III gives the theoretical analysis of flapping resonance. Section IV details the experiment results. The paper is concluded with discussions and future works.

II. DYNAMIC MODEL OF FLAPPING WING ACTUATION

A. *Flapping Wing System for Case Study*

The flapping wing MAV used for experiment validation and case studies in this work is introduced here. As illustrated in (7) in Fig. 1, two flapping wings are directly driven by two 2.5-g, 6-mm brushless DC motors coupled with torsional springs for kinetic energy restoration. Using a gear transmission, the motor was designed to generate reciprocal motion of the wing. The wing was constructed from carbon fiber-reinforced polymer and Mylar membrane. The frame structure, wing stoppers, and spring holders were prototyped by 3-D printing using a multi-purpose transparent resin. A portion of the gear on the load shaft
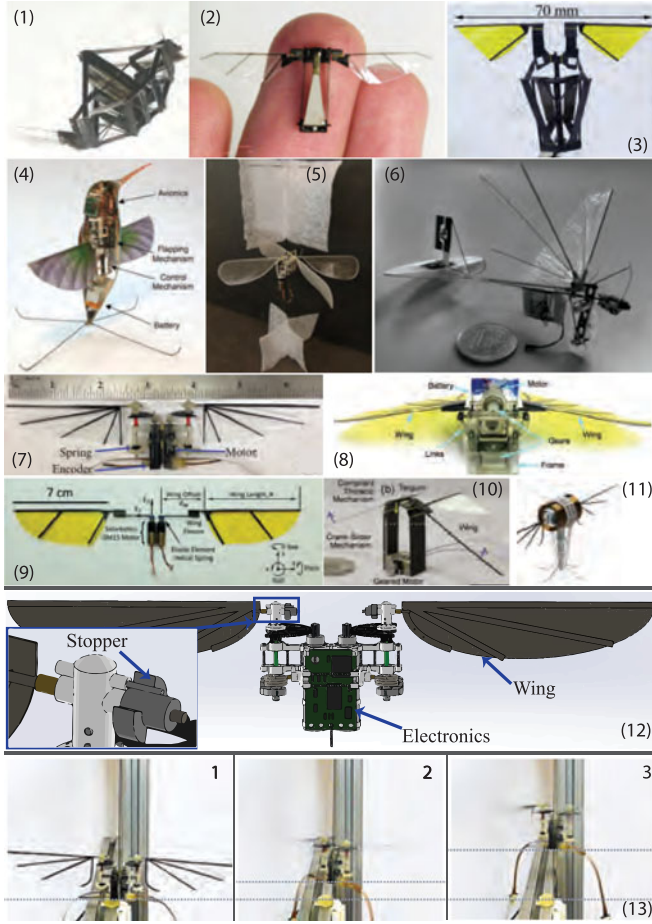
Fig. 1. Flapping wing robots: (1) Berkely MFI [5], (2) Harvard Robobee [6], (3) CMU [7], (4) Nano Humminbird [8], (5) Cornell [9], (6) Delfly [10], (7) Purdue [11], [12], (8) Beetle [13], (9) CMU [14], (10) NTU [15], (11) Purdue [16]. (11) Solidwork model of the FWMAV and the wing stopper. (12) Liftoff sequence of the prototype.
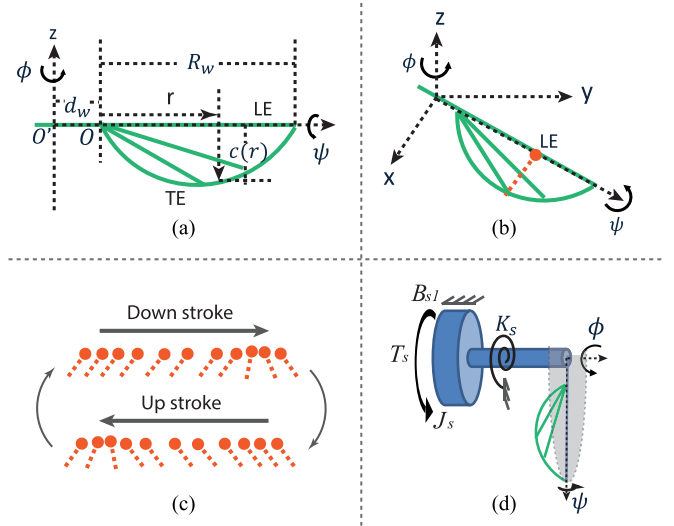

Fig. 2. (a) Parameters of wing shape: R_w is the wing length, O is wing root, i.e., the intersection of leading edge (LE) and trailing edge (TE), $c(r)$ is the chord length at distance r from O, O' is the intersection of stroke axis z and LE, d_w is the wing offset of O from O', stroke angle is ϕ, and rotation angle is ψ. (b) Body xyz coordinate system is fixed to the vehicle airframe. The wing flaps about the ϕ-axis, which remains parallel with the body z-axis. The wing rotation ψ-axis is parallel with respect to the wing leading edge. Wing can also deviate from stroke plane with angle θ, but deviation is not considered here. Rotation is defined to be positive around its axis following right-hand rule. (c) Diagram of typical flapping wing motion projected onto a 2-D plane. Dashed lines indicate the instantaneous position of the wing chord at temporally equidistant points during each half-stroke. Small circles mark the leading edge. Wing moves left to right during downstroke, right to left during upstroke. (d) Diagram of a generalized flapping wing actuation system consisting of applied actuation torque T_s, moment of inertia of rotational elements J_s (including wing), lumped linear damping term $B_s 1$, torsion spring with spring constant K_s, wing with stroke angle ϕ and rotation angle ψ, and nonlinear damping from the wing's aerodynamic damping effects (not shown).

was removed to reduce the weight and moment of inertia. Two miniature ball bearings support each load shaft. A torsion spring was mounted on the bottom of each shaft and oriented in such a way that rotation to one direction compresses one spring and extends the other. The wing was allowed to passively rotate up to a 45° angle limited by a stopper fixed at the proximal end of the wing leading-edge spar. The assembled system with weight of 7.5 g and wing span of 15 cm is capable of taking off with maximum 12 g of lift. As a result, the experiment studies in this work were conducted at scale, and the results can be directly applied with insect/hummingbird-size flapping wing robots.

B. Flapping Wing Aerodynamic Model

The geometric quantities of the wing are defined with parameterization methods detailed in [32]. We have the moment of inertia of the wing with respect to the wing root as

$$J_w = \int_0^{R_w} \rho_w c(r) r^2 dr = \rho_w R_w^3 \bar{c} \hat{r}_2^2 \tag{1}$$

where, as illustrated in Fig. 2(a), wing root is at O, R_w is the wing length, ρ_w is the wing planar density, $c(r)$ is the chord

length at r distance from the wing root O, $\bar{c} = \frac{1}{R_w} \int_0^{R_w} c(r) dr$ is the mean chord length, and $\hat{r}_2^2$ and $\hat{r}_3^3$ are the second and third moment of wing area, respectively, given by $\hat{r}_2^2 = \frac{\int_0^{R_w} c(r) r^2 dr}{\bar{c} R_w^3}$ and $\hat{r}_3^3 = \frac{\int_0^{R_w} c(r) r^3 dr}{\bar{c} R_w^4}$. In consideration of the nonnegligible wing offset d_w, the wing geometric quantities are transformed according to

$$R_w' = R_w + d_w, \bar{c}' = \frac{R_w \bar{c}}{R_w'}, \hat{r}_1^{1'} = \frac{R_w \hat{r}_1^1 + d_w}{R_w'}$$

$$\hat{r}_2^{2'} = \frac{R_w^2 \hat{r}_2^2 + 2 d_w R_w \hat{r}_1^1 + d_w^2}{R_w^{2'}}$$

$$\hat{r}_3^{3'} = \frac{R_w^3 \hat{r}_3^3 + 3 d_w R_w^2 \hat{r}_2^2 + 3 d_w^2 R_w \hat{r}_1^1 + d_w^3}{R_w^{3'}} \tag{2}$$

where $\hat{r}_1^1$ is the first moment of wing area, variables without prime follow the original definitions, and ones with prime are corrected variables with wing offset considered. Once transformed, the primes are dropped for all following modeling steps, in favor of cleaner notations.

A general flapping wing is capable of three-degree-of-freedom (DoF) motion: wing stroke (flapping), wing rotation (pitching), and wing deviation, illustrated in Fig. 2(b). Stroke

(ϕ) is the back-and-forth wing motion defined in the stroke plane. Rotation (ψ) is the angle rotated by wing relative to its rotation axis, generally close and parallel to the leading edge. The deviation is the angle with which the wing rotation axis deviates from the stroke plane, but due to added weight and limited enhancement on the aerodynamic lift, the deviation is usually not incorporated in the vehicle design. Typical two-DoF wing flapping motions are illustrated in Fig. 2(c) with the cut view of flapping wing motion projected onto a 2-D plane.

With a quasi-steady aerodynamic model [1], the instant lift force and aerodynamic damping torque on the wing at time t with wing flapping $\phi(t)$, rotation $\psi(t)$, and angle of attack $\alpha(t)$ [5] are given by

$$F_L(t) = \frac{1}{2}\rho_a \bar{C}_L R_w^3 \bar{c}\hat{r}_2^2 \dot{\phi}^2,$$

$$\tau_d(t) = B_{s2}\dot{\phi}^2 \text{sign}(\dot{\phi}) \tag{3}$$

where ρ_a is the air density, $B_{s2} = \frac{1}{2}\rho_a \bar{C}_D R_w^4 \bar{c}\hat{r}_3^3(S)$ is the aerodynamic damping coefficient, and $\overline{C_L}$ and $\overline{C_D}$ are the mean lift and drag coefficients averaged over one wing stroke, respectively, given by [1]

$$\overline{C_D} = \overline{1.92 - 1.55\cos(2.04\alpha - 9.82)}$$

$$\overline{C_L} = \overline{0.225 - 1.58\sin(2.13\alpha - 7.20)} \tag{4}$$

where the angle of attack is α. The quasi-steady model is adopted here due to the lack of simple closed-form model for unsteady aerodynamics [1].

The center of pressure [5], i.e., the location where the aerodynamic forces acting on the wing, is defined as

$$r_{\text{cp}} = \frac{R_w \hat{r}_3^3(S)}{\hat{r}_2^2(S)} = \frac{\int_0^{R_w} c(r)r^3 \, dr}{\int_0^{R_w} c(r)r^2 \, dr}. \tag{5}$$

C. General Flapping Wing Actuation Model

While the flapping wing system considered here has two DoFs, i.e., wing stroke (flapping) and wing rotation, only flapping motion is actuated, while wing rotates passively due to aerodynamic and inertial forces. The passive wing rotation has been observed in most insect flight to reduce the actuation complexity and the power requirements [17], [33], which has been applied in a number of robotic platforms as well [6], [11], [14]. The passive wing rotation is realized either though flextural hinge [14], [34] or mechanical stopper that limits the free wing rotation up to a desired maximum angle of attack [11].

As shown in Fig. 2(b) and (c) and also in study [1], the passive wing rotation consists mostly of two parts: translation at optimal angle of attack for majority of the stroke motion and rotation to the other extreme during stroke reversals. The angle of attack will not be constant at least during stroke reversals. Hines *et al.* [14] have studied the model of such a two-DoF system.

In order to reveal the underlying flapping resonance, simplifications have been made to reduce the complexity of the dynamics, typically with assumptions of constant angle of attack [14], [27]. In this work, as the passive wing rotation is limited by a stopper to optimal 45° angle of attack during most

of the stroke motion, a constant angle of attack of 45° is assumed. This assumption implies that ideally the wing can rotate instantaneously from 45° to −45°, and vice versa, at the two extremes of stroke reversals to always deliver the constant angle of attack of 45°. Finio *et al.* [27] also assumed fixed angle of attack of 45°, while Hines *et al.* [14] adopted the angle of attack of 90°.

The wing stroke dynamics is more dominant than the wing rotation dynamics. In [27], it was shown that the majority of kinetic energy due to wing movement is stored in the flapping mode, about 50 times larger than that in the rotation mode. As a result, we assume that the behavior of the wing is modeled by a beam damped by quasi-steady aerodynamics, rotating about the stroke axis and resonating with torsional spring, as shown in Fig. 2(d), where the wing stroke angle (ϕ) is driven by the actuator under resonance with torsional spring stiffness (K_s) and passive wing rotation angle (ψ). The behavior of the wing is modeled by

$$J_s\ddot{\phi} + B_{s1}\dot{\phi} + T_a + T_r = T_s \tag{6}$$

where ϕ is the flapping/stroke angle in rad, J_s is the total moment of inertia of rotational elements, B_{s1} is the lumped linear damping coefficients, T_a is the aerodynamic damping torque on the wing as it flaps, T_r is the elastic restoring torque, and T_s is the input torque applied by the actuator. From the aerodynamic model of flapping wing, $T_a = B_{s2}|\dot{\phi}|\dot{\phi}$, where B_{s2} is the aerodynamic damping coefficients. The aerodynamic damping term $B_{s2}|\dot{\phi}|\dot{\phi}$ is estimated based on a quasi-steady aerodynamic model using blade element theory [1]. If the elastic elements can be approximated as linear, $T_r = K_s\phi$, with stiffness K_s. Without loss of generality, input torque can be rewritten as the product of linear input gain K_u and a physical quantity u, i.e., $T_s = K_u u$. Equation (6) becomes

$$J_s\ddot{\phi} + B_{s1}\dot{\phi} + B_{s2}|\dot{\phi}|\dot{\phi} + K_s\phi = K_u u. \tag{7}$$

The system is normally excited with sinusoidal input $u = V_{\text{in}}\cos(\Omega t + \beta)$, where V_{in} is the magnitude, Ω is the angular frequency, and β is the phase.

This general wing actuation model can capture the nonlinear dynamics of motor direct-driven flapping wing [14], [30], [35], piezo-driven flapping wing [27], and even insect wings [17].

D. Flapping Wing Actuation Model With a DC Motor

The flapping wing actuation system with a DC motor is illustrated in Fig. 3. The wing stroke (ϕ) is driven by the DC motor under resonance with torsion spring (K_s), and passive wing rotation (ψ) is limited by the stopper to optimal angle of attack of 45°.

As the inductance of the motor is negligible, similar to [11] and [30], the equation of motion for the DC motor is

$$J_m\ddot{\phi}_m + B_m\dot{\phi}_m = K_a I_a - T_m \tag{8}$$

where J_m is the moment of inertia of the motor rotating elements, ϕ_m is the motor angle, B_m is the damping coefficient of the motor rotating elements, K_a is the torque constant, I_a is the armature current, and T_m is the motor
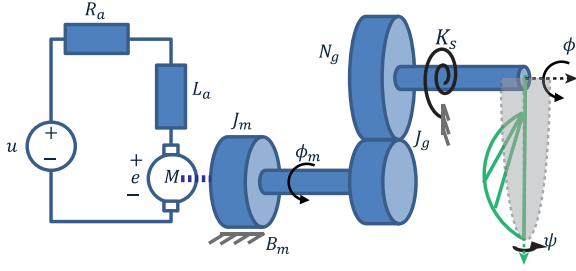
Fig. 3. Diagram of flapping wing actuation system consisting of (1) motor with voltage input u, resistance R_a, inductance L_a, back EMF voltage e, motor moment of inertia J_m, shaft damping B_m, and motor angle ϕ_m; (2) gear with gear ratio N_g, gear moment of inertia J_g; (3) torsion spring with stiffness K_s; and (4) wing with stroke angle ϕ, rotation angle ψ, and parameters defined in Fig. 2(a).

load torque. $I_a = \frac{u - K_a \dot{\phi}_m}{R_a}$, with u being the input voltage to the motor and R_a being the resistance of the motor. Defining $B_{m1} = B_m + \frac{K_a^2}{R_a}$, we have

$$J_m \ddot{\phi}_m + B_{m1} \dot{\phi}_m = \frac{K_a}{R_a} u - T_m. \tag{9}$$

With gear transmission, we have $\phi_m = N_g \phi_l$, $\eta_g N_g T_m = T_l$, with N_g being the gear ratio, ϕ_l being the load angle, T_l being the load torque, and η_g being the gear efficiency. Then, the motor dynamics becomes

$$J_e \ddot{\phi}_l + B_e \dot{\phi}_l = K_u u - T_l \tag{10}$$

where the effect moment of inertia $J_e = \eta_g N_g^2 J_m$, effective damping $B_e = B_{s1} = \eta_g N_g^2 (B_m + \frac{K_a^2}{R_a})$, and input gain $K_u = \eta_g N_g \frac{K_a}{R_a}$.

Directly driving the wing using geared motor with coupled parallel torsion spring, as shown in Fig. 3, we have $T_l = J_w \ddot{\phi}_w + B_{s2} \dot{\phi}_w |\dot{\phi}_w| + K_s \phi_w$ and $\phi_l = \phi_w = \phi$; thus

$$J_s \ddot{\phi} + B_{s1} \dot{\phi} + B_{s2} |\dot{\phi}| \dot{\phi} + K_s \phi = K_u u \tag{11}$$

where the total moment of inertia is $J_s = N_g^2 J_m + J_w + J_g$. Compared with the general flapping wing actuation system model (7), in the case of DC motor, input torque $T_s = K_u u$ is different from the motor torque T_m.

As a special case, for the DC motor with fast current feedback control loop, the input to the system is the regulated output current I_a from the current control loop. The differences of the corresponding system parameters for (11) are $B_{s1} = \eta_g N_g^2 B_m$, $K_u = \eta_g N_g K_a$, and $u = I_a$.

E. Flapping Wing Actuation Model for Other Types of Systems

In [27], the actuation based on piezoelectric cantilever beam delivers an oscillatory mechanical input to a four-bar transmission, converting linear motion of the tip of the actuator to flapping motion of the wings. Each wing is attached to the transmission through a flexure hinge that acts as a torsion spring, allowing the wing to rotate passively due to aerodynamic and inertial forces as it flaps. Under the assumption of small displacements, the four-bar transmission can be approximated

as a linear transmission, which effectively functions similarly to the gear transmission of the DC motor case. With the model of a piezoelectric cantilever beam as a spring–mass subsystem, the overall wing actuation model with a piezoelectric cantilever beam can still be accurately captured with the general model in (7), as shown in [27].

Flapping wing insects have two types of muscles actuating their wings: synchronous and asynchronous muscles. The synchronous muscles are mostly responsible for modulating the wing rotation and fine-tuning the flapping motion, while asynchronous muscles provide the majority of power for flapping motion, indirectly moving the wings by exciting a resonant mechanical load in the body structure. The asynchronous muscles are analogous to the DC motor and torsion spring in previous section. Biological study in [17] modeled the muscle elasticity and its force-extension relation as elastic polymers such as rubber, and the restoring force fr can be described as

$$fr = E_0 A_0 (\beta - \beta^{-2}) \tag{12}$$

where E_0 is the elastic modulus of the muscle, A_0 is the cross section of the unstrained muscle, and β is the extension ratio b/b_0, where b and b_0 are the length of the strained and unstrained muscle relative to the equilibrium positions, respectively. For small extension ratios, the expression $\beta - \beta^{-2}$ reduces to $3\Delta b/b_0$, and the muscle can be approximated as a linear spring similar to the torsion spring in the DC motor case. Without a good understanding of the unsteady aerodynamics of flapping wing at the time, Greenewalt[17] modeled the flapping wing aerodynamics directly as an unknown linear damping term. Incorporating the aerodynamic modeling from previous section, the general model of (7) applies to the biological flapping wing system as well.

III. Effects of Resonance on Flapping Wing Response

Dynamics of the flapping wing actuation system (7) is nonlinear, and its response cannot, in general, be expressed as simple analytic formulas. It is necessary to numerically simulate the dynamics to get the response.

To facilitate the analysis, especially of the influences of resonance and system parameters on the system response, linearization methods were regularly utilized [27], [30], [36]. In [27], the nonlinear aerodynamic damping was linearized about an operating point of maximum drag and fixed 45° angle of attack, while in [30] and [36], a linear damping coefficient is defined to approximate the nonlinear aerodynamic damping effect to provide the same average power over a wingbeat period.

In order to provide a theoretical basis for linear approximation and quantify the associated errors, we use a nonlinear perturbation method, i.e., the method of multiple scales [37], [38], to analyze the nonlinear dynamics and obtain analytical predictions of forced responses of the dynamics (7). The closed-form solutions capture the nonlinear vibration response as functions of system parameters, revealing insights about how system parameters and resonance affect the steady-state response and energetics of flapping wing.

A. Nonlinear Analysis of Flapping Wing Response

Excited with sinusoidal input $u = V_{\text{in}}\cos(\Omega t)$ with amplitude V_{in} and frequency Ω, the equation of motion (7) can be rewritten in the following dimensionless form:

$$\ddot{\phi} + \omega_n^2 \phi = -2\epsilon\mu\dot{\phi} - \epsilon|\dot{\phi}|\dot{\phi} + E(t) \qquad (13)$$

which represents a forced oscillator with a quadratic damping and a spring. The natural frequency or primary resonance is $\omega_n = \sqrt{\frac{K_s}{J_s}}$. $\epsilon = \frac{B_{s2}}{J_s}$ is a small dimensionless perturbation parameter [37]. $\mu = \frac{B_{s1}}{2J_s\epsilon}$ is the normalized linear damping coefficient. $E(t) = \frac{K_u}{J_s}u = \epsilon k\cos(\omega_n t + \epsilon\sigma t)$ is the input excitation, where $\Omega = \omega_n + \epsilon\sigma$ and $k = \frac{K_u V_{\text{in}}}{J_s\epsilon}$. $\sigma = O(1)$ is the detuning parameter [37], which quantifies the nearness of Ω to ω_n.

The approximate solution of (7) near ω_n can be obtained using the method of multiple scales [37]. Specifically, we first define new time scales $T_i = \epsilon^i t$, $i = 0, 1, 2\ldots$, and the solution has the form

$$\phi(t, \epsilon) = \phi_0(T_0, T_1) + \epsilon\phi_1(T_0, T_1) + \ldots. \qquad (14)$$

Then, the first-order approximation of the solution is

$$\phi_0 = A\cos(\omega_n T_0 + B(T_1)) + O(\epsilon) \qquad (15)$$

which means the response of the system is approximately sinusoidal with approximation error quantified by parameter ϵ. In this work, with the parameters of the DC motor-driven flapping wing system, $\epsilon = O(0.1)$.

The amplitude A and phase B are solved by two ordinary differential equations

$$\dot{A} = -\mu A - \frac{4}{3\pi}A|A|\omega_n + \frac{k}{2\omega_n}\sin(\gamma)$$

$$A\dot{\gamma} = A\sigma - \frac{k}{2\omega_n}\cos(\gamma) \qquad (16)$$

where $\gamma = \sigma T_1 - B$.

The steady-state solution is solved by setting time derivatives to zeros, i.e., $\dot{A} = 0$ and $\dot{\gamma} = 0$; we then have

$$A^2\left[\left(\mu + \frac{4}{3\pi}A|A|\omega_n\right)^2 + \sigma^2\right] = \frac{k^2}{4\omega_n^2} \qquad (17)$$

which is commonly called frequency-response equation. The steady-state amplitude of the response A can be solved given the driving frequency Ω (or σ).

When the system is driven at natural frequency, i.e., $\sigma = 0$ and $\Omega = \omega_n$, then the amplitude prediction $A = A_n$ is

$$A_n = \frac{-\mu + \sqrt{\mu^2 + \frac{8k}{3\pi}}}{\frac{8}{3\pi}\omega_n} \qquad (18)$$

which can be transformed into

$$A_n\omega_n = \frac{1}{2B_2}\left(\sqrt{B_{s1}^2 + 4B_2 V_{\text{in}}K_u} - B_{s1}\right) \qquad (19)$$

with the original system parameters and lumped parameter $B_2 = B_{s2}\frac{8}{3\pi}$.

With the first-order approximation of the solution in (15), the stroke-averaged power drained by aerodynamic damping is

$$\overline{P_d} = \frac{1}{T}\int_T B_{s2}\dot{\phi}|\dot{\phi}|\dot{\phi}dt = \frac{4}{3\pi}B_{s2}(A\Omega)^3 + O(\epsilon^3) \qquad (20)$$

the total power is

$$\overline{P_{\text{total}}} = \frac{1}{T}\int_T uI_a dt$$

$$= \frac{1}{2}\left(\frac{V_{\text{in}}}{R_a} - N_g\frac{K_a}{R_a}\Omega A\right)V_{\text{in}} + O(\epsilon) \qquad (21)$$

and the mean efficiency is

$$\overline{E_{\text{ff}}} = \frac{\overline{P_d}}{\overline{P_{\text{total}}}} = \frac{B_{s2}\frac{8}{3\pi}(A\Omega)^3 + O(\epsilon^3)}{\left(\frac{V_{\text{in}}}{R_a} - N_g\frac{K_a}{R_a}A\Omega\right)V_{\text{in}} + O(\epsilon)}. \qquad (22)$$

Substituting $A_n\omega_n$ from (19) gives the closed-form formulas for energetics of flapping wing.

B. Linear Approximation of Flapping Wing Response

The nonlinear analysis above well captures the system response excited at/near natural frequency. We have $\epsilon = \frac{B_{s2}}{J_s}$ to quantify approximation errors when sinusoidal output is assumed as well.

A typical second-order resonant system can, in addition, be characterized by damped natural frequency and peak frequency. To facilitate the definition of these frequencies and to characterize the associated system response, here, we adapt the linear approximation methods from [27], [30], and [36], despite the differences on actuation and dynamics. Analysis of the system response especially at damped natural frequency and peak frequency was performed. Moreover, we quantify the errors and identify the limitations of the linear approximation based on the results of previous nonlinear analysis.

When the system is excited with sinusoidal input $u = V_{\text{in}}\cos(\Omega t)$ with amplitude V_{in} and frequency Ω, as shown in [30] and [36], a linear damping B_1 can be defined to capture the nonlinear aerodynamic damping effects to provide the same average power over a wingbeat period, i.e., $\frac{1}{T}\int_T B_1\dot{\phi}\dot{\phi}dt = \frac{1}{T}\int_T B_{s2}\dot{\phi}|\dot{\phi}|dt$. With the assumption of sinusoidal response, it can be shown that $B_1 = B_{s2}\frac{8}{3\pi}\Omega A = B_2\Omega A$.

To quantify approximation errors, in this work, the criterion for evaluating the linear approximation accuracy is defined as the time-averaged squared error over one wingbeat for the nonlinear damping torque. With the assumption of sinusoidal output, we have

$$Err = \frac{1}{T}\int_T (B_1\dot{\phi} - B_{s2}\dot{\phi}|\dot{\phi}|)^2 dt$$

$$= \frac{A^2\Omega^2}{2}(B_1^2 + \frac{3}{4}B_{s2}^2 A^2\Omega^2 - \frac{16}{3\pi}B_1 B_{s2}A\Omega) \qquad (23)$$

which is minimized to

$$Err_{\text{min}} = (3/4 - (8/3/pi)^2)B_{s2}^2\Omega^2 A^2 \approx 0.03(B_{s2}\Omega A)^2 \qquad (24)$$

with $B_1 = B_{s2} \frac{8}{3\pi} \Omega A = B_2 \Omega A$. This showed that the equivalent average power approach of [30] and [36] minimized the wingbeat-averaged squared approximation error as well.

Essentially, the nonlinear aerodynamic damping is linearized here, not about an operating point, but with steady state of the response, as B_1 is a function of the frequency Ω and steady-state amplitude of the response A. In comparison, Finio *et al.* [27] had the nonlinear aerodynamic damping linearized about an operating point of maximum drag (in the middle of the half stroke with maximum flapping velocity) and fixed $45°$ angle of attack, giving a "worst-case" estimate for aerodynamic damping. The approach in [27] could lead to conservative estimates of the flapping damping effects: the effective linear damping coefficient in [27] is $3\pi/4 \approx 2.356$ times of current value B_1.

With the linear damping B_1, the equation of motion (7) can be approximated by the following linear dynamics:

$$J_s \ddot{\phi} + B_l \dot{\phi} + K_s \phi = K_u u \qquad (25)$$

with the transfer function as

$$G(s) = \frac{\Phi(s)}{U(s)} = \frac{K_u}{J_s s^2 + B_l s + K_s}$$
$$= \frac{K_0}{s^2 + 2\xi \omega_n s + \omega_n^2} \qquad (26)$$

where $K_0 = \frac{K_u}{J_s}$, natural frequency $\omega_n = \sqrt{(K_s/J_s)}$, $B_l = B_{s1} + B_2 \Omega A$, and damping ratio $\xi = \frac{B_l}{2\sqrt{J_s K_s}}$.

From linear system theory, we have the following definition for frequencies related to resonance:
1) *Natural frequency:* $\omega_n = \sqrt{(K_s/J_s)}$.
2) *Damped natural frequency:* $\omega_d = \omega_n \sqrt{1 - \xi^2}$.
3) *Peak frequency:* ω_p, for moderately underdamped ($\xi < 1/\sqrt{2}$) second-order harmonic oscillator having its maximum gain $|G(\Omega j)|_{\max}$ when driven by a sinusoidal input. All the wings tested in this study did not exceed this critical value for damping ratio.

The response is typically what to be determined and unknown in advance. This linear model will not be useful for predicting the steady-state response or even running simulation, as its own parameters depend on the response. At particular characteristic frequencies, however, this difficulty can be alleviated. Next, we test the system responses driven at different frequencies. Here, we use A_i to represent the amplitude of system response at frequency ω_i, with $i = n, d, p$ being natural frequency, damped natural frequency, and peak frequency, respectively.

1) Natural Frequency: When the system is driven at natural frequency, i.e., $\Omega = \omega_n$, we can substitute the closed-form solution of $A_n \omega_n$ (19) into B_1 for the linear model (25) and obtain

$$J_s \ddot{\phi} + \frac{1}{2} \left(B_{s1} + \sqrt{B_{s1}^2 + 4B_2 V_{in} K_u} \right) \dot{\phi} + K_s \phi = K_u u \qquad (27)$$

where at natural frequency, $\angle G(\omega_n j) = -\frac{\pi}{2}$ and $A_n = V_{in}|G(\omega_n j)| = \frac{V_{in} K_u}{\frac{1}{2}\left(B_{s1} + \sqrt{B_{s1}^2 + 4B_2 V_{in} K_u}\right)\omega_n}$, which is

rewritten as

$$A_n \omega_n = \frac{2V_{in} K_u}{B_{s1} + \sqrt{B_{s1}^2 + 4B_2 V_{in} K_u}}. \qquad (28)$$

Equation (28) can be shown to be the same as (19), which connects the nonlinear analysis with the linear approximation. It shows that the linear approximation method is accurate at least when the system is driven at natural frequency. The approximation error can also be characterized with the same parameters $\epsilon = \frac{B_{s2}}{J_s}$ and the big O notation used in the nonlinear analysis.

2) Damped Natural Frequency and Peak Frequency: When the system is driven at other frequency Ω, i.e., $u = V_{in} cos(\Omega t)$, we have

$$\phi = |G(\Omega j)| V_{in} cos(\Omega t + \angle G(\Omega j)) \qquad (29)$$

where the response amplitude is

$$A = |G(\Omega j)| V_{in} = \frac{K_u V_{in}}{\sqrt{(K_s - J_s \Omega^2)^2 + B_l^2 \Omega^2}}. \qquad (30)$$

Equation (30) can be rewritten as

$$B_2^2 \Omega^4 A^4 + 2B_{s1} B_2 \Omega^3 A^3 + (K_s^2 + J_s^2 \Omega^4) A^2$$
$$+ (B_{s1}^2 - 2J_s K_s)\Omega^2 A^2 - (K_u V_{in})^2 = 0 \qquad (31)$$

which is a nonlinear function of amplitude and frequency. A numerical solution can be obtained for amplitude A, given driving frequency Ω, even though a simple closed-form solution may not exist.

For the special case when $B_{s1} \approx 0$, e.g., current-controlled DC motor with low frictional damping on the shaft and flapping wing animals, however, (31) becomes

$$c_{01} A^4 + c_{02} A^2 + c_{03} = 0 \qquad (32)$$

where $c_{01} = B_2^2 \Omega^4$, $c_{02} = (K_s - J_s \Omega^2)^2$, and $c_{03} = -(K_u V_{in})^2$. Given frequency Ω, the closed-form solution for (32) is

$$A = \sqrt{\frac{-c_{02} + \sqrt{c_{01}^2 - 4c_{01} c_{03}}}{2c_{01}}}. \qquad (33)$$

For the system response driven at damped natural frequency, $\Omega = \omega_d = \omega_n \sqrt{1 - \xi^2}$, the numerical solution for amplitude A_d can be obtained from (31).

When the system is driven at peak frequency, i.e., $\Omega = \omega_p$, from traditional linear theory, peak frequency is typically defined as $\omega_p = \omega_n \sqrt{1 - 2\xi^2}$, with maximum gain $|G(\Omega j)|_{\max} = \frac{K_u}{2\xi\sqrt{1-\xi^2}}$. Here, we show that this is actually not the case, as damping term B_1, B_l, and ξ are functions of resulting amplitude A and driving frequency Ω. We need to derive the maximum amplitude and peak frequency accordingly.

As B_l is also a function of A and Ω, we have $\frac{\partial B_l}{\partial \Omega} = B_2 A + B_2 \Omega \frac{\partial A}{\partial \Omega}$. The maximum amplitude is obtained by taking the partial derivative of (30) with respect to Ω and setting $\frac{\partial A}{\partial \Omega} = 0$, and we have

$$c_{11} \omega_p^2 + c_{12} \omega_p + c_{13} = 0 \qquad (34)$$

where $c_{11} = 2(B_2^2 A_p^2 + J_s^2)$, $c_{12} = 3B_{s1}B_2 A_p$, and $c_{13} = (B_{s1}^2 - 2J_s K_s)$. If A_p is known, we can solve the peak frequency as

$$\omega_p = \frac{-c_{12} + \sqrt{c_{12}^2 - 4c_{11}c_{13}}}{2c_{11}}. \tag{35}$$

With (31) and (34), we cancel out the A^3 term and have

$$c_{21}A_p^4 - c_{22}A_p^2 + c_{23} = 0 \tag{36}$$

where $c_{21} = B_2^2 \omega_p^4$, $c_{22} = (3K_s^2 + B_{s1}^2 \omega_p^2 - J_s^2 \omega_p^4 - 2J_s K_s \omega_p^2)A_p^2$, and $c_{23} = 3(K_u V_{\text{in}})^2$. If ω_p is known, we can solve the maximum amplitude as

$$A_p = \sqrt{\frac{c_{22} - \sqrt{c_{21}^2 - 4c_{21}c_{23}}}{2c_{21}}}. \tag{37}$$

However, A_p and ω_p need to be solved together. The system of nonlinear equations consisting of (34) and (36) with two variables $[\omega_p, A_p]$ can be solved numerically, for example, with the MATLAB function fsolve. To speed up the convergence, the initial solution can be set to $[\omega_n, A_n]$ according to closed-form solution (19) and $\omega_n = \sqrt{(K_s/J_s)}$.

3) Summary of Analytical Results: The analytic formulas for predicting characteristic frequencies and system responses are summarized here.

1) At natural frequency $\omega_n = \sqrt{(K_s/J_s)}$, the closed-form solution for amplitude A_n is

$$A_n \omega_n = \frac{1}{2B_2}\left(\sqrt{B_{s1}^2 + 4B_2 V_{\text{in}}K_u} - B_{s1}\right), \text{ or}$$

$$A_n \omega_n = \frac{2V_{\text{in}}K_u}{B_{s1} + \sqrt{B_{s1}^2 + 4B_2 V_{\text{in}}K_u}} \tag{38}$$

and the linear model is

$$J_s \ddot{\phi} + \frac{1}{2}\left(B_{s1} + \sqrt{B_{s1}^2 + 4B_2 V_{\text{in}}K_u}\right)\dot{\phi}$$
$$+ K_s \phi = K_u u. \tag{39}$$

2) At damped natural frequency $\omega_d = \omega_n\sqrt{1 - \xi^2}$, the numerical solution for amplitude A_d can be obtained from

$$B_2^2 \omega_d^4 A_d^4 + 2B_{s1}B_2 \omega_d^3 A_d^3 + (K_s^2 + J_s^2 \omega_d^4)A_d^2$$
$$+ (B_{s1}^2 - 2J_s K_s)\omega_d^2 A_d^2 - (K_u V_{\text{in}})^2 = 0. \tag{40}$$

3) At peak frequency, ω_p and A_p can be solved numerically from the following system of nonlinear equations:

$$c_{11}\omega_p^2 + c_{12}\omega_p + c_{13} = 0$$
$$c_{21}A_p^4 - c_{22}A_p^2 + c_{23} = 0 \tag{41}$$

where $c_{11} = 2(B_2^2 A_p^2 + J_s^2)$, $c_{12} = 3B_{s1}B_2 A_p$, $c_{13} = (B_{s1}^2 - 2J_s K_s)$, $c_{21} = B_2^2 \omega_p^4$, $c_{22} = (3K_s^2 + B_{s1}^2 \omega_p^2 - J_s^2 \omega_p^4 - 2J_s K_s \omega_p^2)A_p^2$, and $c_{23} = 3(K_u V_{\text{in}})^2$.

4) Flapping wing energetics: The stroke-averaged power requirement of flapping wing drained by aerodynamic damping is

$$\overline{P_d} = \frac{4}{3\pi}B_{s2}(A\Omega)^3 + O(\epsilon^3) \tag{42}$$

the total power is

$$\overline{P_{\text{total}}} = \frac{1}{2}\left(\frac{V_{\text{in}}}{R_a} - N_g \frac{K_a}{R_a}\Omega A\right)V_{\text{in}} + O(\epsilon) \tag{43}$$

and the mean efficiency is

$$\overline{E_{\text{ff}}} = \frac{\overline{P_d}}{\overline{P_{\text{total}}}} = \frac{B_{s2}\frac{8}{3\pi}(A\Omega)^3 + O(\epsilon^3)}{\left(\frac{V_{\text{in}}}{R_a} - N_g \frac{K_a}{R_a}A\Omega\right)V_{\text{in}} + O(\epsilon)}. \tag{44}$$

4) Theoretical Analysis: The term resonant frequency has been loosely used, and referring to different quantities by various research communities, it is often referred to peak frequency, corresponding to the largest flapping angle from experiment frequency response. However, resonant frequency is also defined to be the natural frequency in the context of nonlinear vibration. To avoid this confusion, we use natural frequency and peak frequency instead. Only when the damping is sufficiently small (e.g., < 0.1), the three frequencies come close to each other. Flapping wing normally has sufficient large damping due to aerodynamic damping, but still mostly underdamped.

The widely adopted method to identify and validate the resonance of the system is by conducting a frequency sweep, during which the wing is driven by a sinusoidal voltage input with different frequencies from a range of interest [6], [14]. The steady-state amplitudes of the responses in terms of flapping angle will be compiled together and plotted with respect to input frequencies. The same can be done in terms of velocity of response and mean lift with respect to frequencies. In the current research among flapping wing micro air vehicle (FWMAV) community, the relationships were not clear among natural frequency, damped natural frequency, peak frequency, the maximum flapping amplitudes, maximum lift, and maximum efficiency. Here, the relationship will be first shown with theoretical analysis and then verified with experiment results.

From the modeling and analysis above, we have following observations.

1) The peak value of flapping angle in frequency response does not correspond to natural frequency of the system and $\omega_p < \omega_n$, unless ξ is really small, which is generally not true for high power and high damping flapping motion. The peak value of the flapping angular velocity, however, corresponds to natural frequency ω_n. The transfer function from input to velocity indicates that $G_v(s) = \frac{V(s)}{U(s)} = \frac{K_u s}{J_s s^2 + B_l s + K_s}$ with $|G_v(\omega j)| = \frac{K_u \omega}{\sqrt{(K_s - J_s \omega^2)^2 + B_l^2 \omega^2}}$, which reach maximum when $\omega = \omega_n$.

2) Maximum lift occurs when driving the system at natural frequency, not the peak frequency. As $\overline{F_L} = \frac{1}{4}\rho_a \overline{C_L} R_w^3 \bar{c}\hat{r}_2^2(S)(A\Omega)^2$, where $A\Omega$ is the magnitude of the flapping angular velocity, maximum lift happens at the peak value of the flapping angular velocity, which occurs at ω_n, as discussed in (1).

3) Maximum efficiency is achieved when the system is driven at natural frequency, not the peak frequency. As the efficiency is defined to be $\overline{E_{\text{ff}}} = \frac{\overline{P_{\text{out}}}}{P_{\text{total}}} \approx \frac{B_{s2}\frac{8}{3\pi}(A\Omega)^3}{\left(\frac{V_{\text{in}}}{R_a} - N_g \frac{K_a}{R_a}A\Omega\right)V_{\text{in}}}$, the maximum efficiency happens for maximum velocity $A\Omega$, thus at resonance ω_n.

As a result, when driving the system at natural frequency ω_n (not peak frequency ω_p), we expect that the maximum lift, maximum efficiency, and maximum velocity (not amplitude) should be achieved for the flapping wing system. The correct method to identify and validate the resonance of the system is by conducting a frequency sweep, after which the frequency corresponding to the maximum value of the steady-state magnitude of the flapping velocity is the natural frequency of the system. Driving the system at this natural frequency, the maximum lift and maximum efficient will be achieved.

IV. EXPERIMENT RESULTS

The simulations and experiments aim to justify following simplifications.

1) *Assumption 1:* With reasonable accuracy, the quasi-steady aerodynamic model can capture the effects of the aerodynamic force on the wing exerted by unsteady aerodynamics.

2) *Assumption 2:* With reasonable accuracy, the two-DoF dynamics of flapping wing with passive wing rotation can be simplified to the one-DoF dynamic model.

3) *Assumption 3:* With reasonable accuracy, the response of the system driven by sinusoidal input can be well approximated as sinusoidal.

Moreover, the goal is to validate the modeling and analysis from previous sections.

A. Materials and Methods

The simulations and experiments were conducted, as a case study, on an FWMAV with two independent, motor-driven flapping wing subsystems, as shown in (7) in Fig. 1. For ease of instrumentation, the flapping wing subsystem was separately mounted onto the single-wing testing setup. The block diagrams of the single-wing testing setup are shown in Fig 4. FAULHABER Brushless DC-Servomotors 0620B has following parameters: nominal voltage 6 V, resistance $R_a = 8.8\,\Omega$, torque constant $K_a = 1.09\text{e-}3$ N·m/A, moment of inertia $J_m = 9.5\text{e-}10$ kg·m^2, and friction damping coefficient $B_m = 9.74\text{e-}9$ N·m·s/rad. The gear ratio is 10, with moment of inertia $J_g = 5\text{e-}9$ kg·m^2, and efficiency $\eta_g = 0.8$. Parameter estimations and system identification were specified in [11]. Simulations and experiments were tested for a total of ten wings. The tested wings have different geometries, as shown in Fig. 5. The wing consists of wing frame and wing membrane attached with polyurethane adhesive. The wing frame is extremely strong and light carbon fiber-reinforced polymer formed using unidirectional carbon fiber segments impregnated with an epoxy binder. The wing shape for the veins and spars of the wing frame was constrained by a silicone modeling process, common for constructions of fiber-reinforced polymers. The wing membrane is 3-μm-thin BoPET(Mylar) sheet trimmed to the wing shape. Carbon fiber rod was fitted to the wing leading edge with cyanoacrylate adhesive to provide stopper attachment and shaft for wing rotation. Parameters of the ten different wings are detailed in Table I.
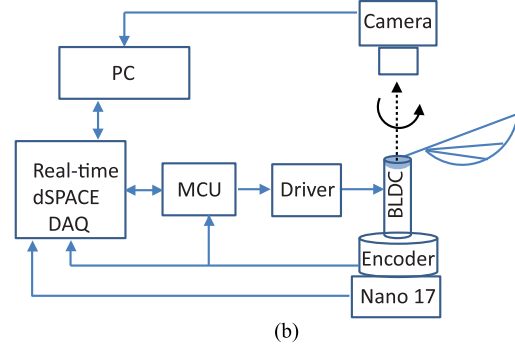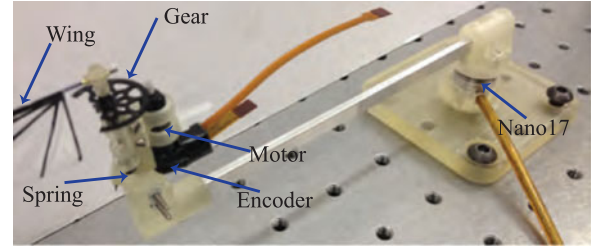
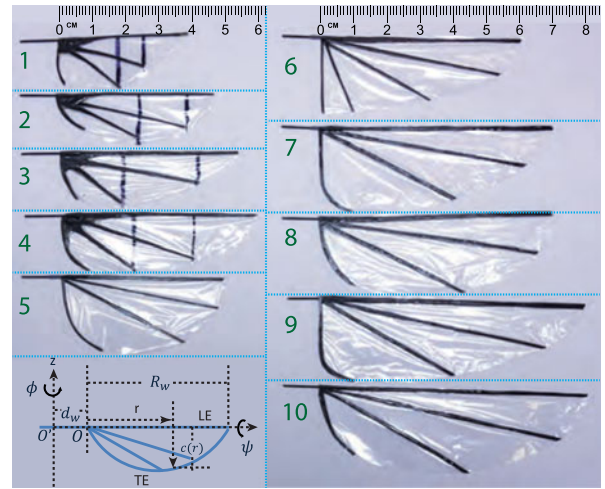Fig. 4. (a) Single-wing experiment setup with force measurement. (b) Block diagram of the experiment setup.

Fig. 5. Ten wings tested with the experiment setup.

All experiments were recorded by real-time dSPACE DS1103 PPC DAQ Board with a sampling frequency $f_s = 5$ kHz. The brushless DC motor three-phase commutation was implemented on a 72-MHz cortex M3 board (NXP Semiconductors, San Jose, CA, USA) at the rate of 50 kHz. The three-phase drive electronics was custom-made for the motor. The wing stroke angle was measured with motor magnetic encoder at the bottom of the motor (FAULHABER Brushless DC-Servomotors 0620B) with 256 counts/rev and calculated according to the gear transmission with gear ratio of 10:1, which gives total $2\pi/2056$ rad resolution on angle measurement. The wing stroke angular velocity is calculated with the simple first-order Euler method. The encoder reading was recorded with the encoder interface on the dSPACE DAQ system along with the force measurements. All the measurement data are synchronized to be recorded real

TABLE I
WING PARAMETERS

Wing	m	R_w	d_w	$\bar{c}$	$\hat{r}_2$	$\hat{r}_3$	J_w	f_n
1	42	47.0	12	8.2	0.61	0.67	34 045	35.98
2	40	50.0	7	9.5	0.65	0.69	31 378	36.41
3	64	55.0	7	9.6	0.59	0.64	66 629	31.76
4	60	58.5	6.5	9.8	0.58	0.67	69 173	31.49
5	54	51.0	7	17.3	0.59	0.64	48 983	33.85
6	66	59.0	7	14.1	0.55	0.63	68 462	31.57
7	85	67.0	7	17.9	0.54	0.63	111 295	27.83
8	103	72.0	12	16.7	0.60	0.65	193 639	23.29
9	88	80.0	10	17.5	0.55	0.63	169 452	24.39
10	88	77.0	7	18.2	0.57	0.67	171 147	24.30

Note: Spring stiffness is $K_s = 0.00588$ N·m/rad. Parameters are corrected with wing offsets. Units of parameters are m (mg), R_w (mm), d_w (mm), $\bar{c}$ (mm), J_w (mg·mm^2), and f_n (Hz). $\hat{r}_2$ and $\hat{r}_3$ are unitless.

time at 5000 Hz. Force measurement was performed using a six-component force/torque transducer (Nano17, ATI Ind. Automation). Due to limited resolution of Nano17 (0.3-g resolution on the force and 1/64-N·mm resolution on the torque measurement), a rigid 150-mm beam setup was used to amplify the lift measurement, as shown in Fig. 4. The improved resolution was about 0.0106 g. The force sensor and beam setup was calibrated with precision weights of 0.1, 0.5, 5, and 20 g and verified the resolution of at least 0.03 g. When calculating the time-averaged force, sufficient numbers of wing-beat cycles at steady state were averaged to guarantee the reliability of the results. The raw data were filtered with a cutoff frequency of 150 Hz. The power source used during experiments is a DC power supply HY-5003 from MASTECH, with current and voltage measurements accurate up to 0.01 A and 0.1 V, respectively.

All numerical simulations were implemented with MATLAB ode45 solver, dynamic models (11) or (39), and parameters specified above.

B. Spring Modeling and Testing

The characterization of elastic elements is essential for design and validation of flapping resonance. For torsion springs (from McMaster–Carr) used in this study, the theoretical model of the spring stiffness is given by

$$K_s = \frac{Ed^4}{64Dn} \tag{45}$$

with wire diameters d, outer diameter D, Young's modulus E, and the number of winding n.

The linearity of the torsional spring is validated experimentally by measuring the spring torque at different angular positions. The corresponding experimental setup is shown in Fig. 6(a). As an example, for one torsional spring with wire diameters $d = 0.3$ mm, outer diameter $D = 2.67$ mm, Young's modulus $E = 193$ Gpa, and the number of winding $n = 4.25$, the experiment result is shown in Fig. 6(b). The spring torque is shown to be proportional to the angular position from $-75°$ to $75°$ with good linearity, and the measured spring stiffness

$K_s = 0.0019$ matches well with the theoretical calculation $K_s = 0.002$.

Sixteen torsion springs with different geometries and spring stiffness from McMaster–Carr were tested. The measured and predicted spring stiffness were plotted together in Fig. 6(c) to show consistent matches of spring model (45) and experiment testing.

C. Model Validation

First, we demonstrate that the nonlinear model (11) and linear model (39) capture the real system with reasonable accuracy. The modeling errors between the real system and the nonlinear model (11) are mainly due to the one-DoF simplification and quasi-steady aerodynamic model. The linear approximation introduces additional errors, as specified by (23). The numerical simulation of the nonlinear model (11) and linear approximation (39) and the experiment response are compared in Fig. 7(a) for wing #6 driven at 6 V, as an example. When simulating the linear model (25), natural frequency and amplitude solution (38) were used for parameter B_l, as the amplitude was unknown in advance. Fig. 7(a) demonstrates the feasibility of the nonlinear and linear modeling, despite the simplifications. Fig. 7(b) illustrates the working mechanism of the linear approximation of damping torques. The linear model approximates the nonlinear damping torque with a linear damping torque. The approximation error is compensated by the difference in the conservative torques from the not-perfect cancellation of the inertial torque and the spring torque. Fig. 7(c) shows the limitations of the linear approximation model with fixed damping coefficient B_l. As the operating frequency deviated from the natural frequency of the system, the modeling errors grew larger. Understanding the assumptions, errors sources, and limitations is important for proper use of the proposed models.

Second, we show that system responses at natural frequency and peak frequency can be predicted with precision by the closed-form solutions (38) and analytic formulas (41), respectively. For sinusoidal inputs at corresponding system natural frequencies, the steady-state amplitudes of the responses from numerical simulations of the nonlinear model (11) were extracted for all ten wings. The amplitude predictions from (38) were compared with simulated ones in the upper plots of Fig. 7(d). Similarly, for peak frequencies, results from simulations and solutions of (41) were compared in the lower plots of Fig. 7(d). Fig. 7(d) illustrated consistent matches between simulations and amplitude predictions for all ten wings. Similar results can be obtained for the formula of damped natural frequency (40), which are not detailed here.

Finally, to verify the assumption of the sinusoidal response, the fast Fourier transforms of the input voltages and output flapping motions are shown in Fig. 7(e) for experiment and in Fig. 7(f) for simulation. The input and output were scaled to unity and plotted together for better comparison. For experiment, a sinusoidal input with amplitude 6 V and at natural frequency was applied to the DC motor, and the flapping wing motion was recorded with the motor encoder. For simulation, a
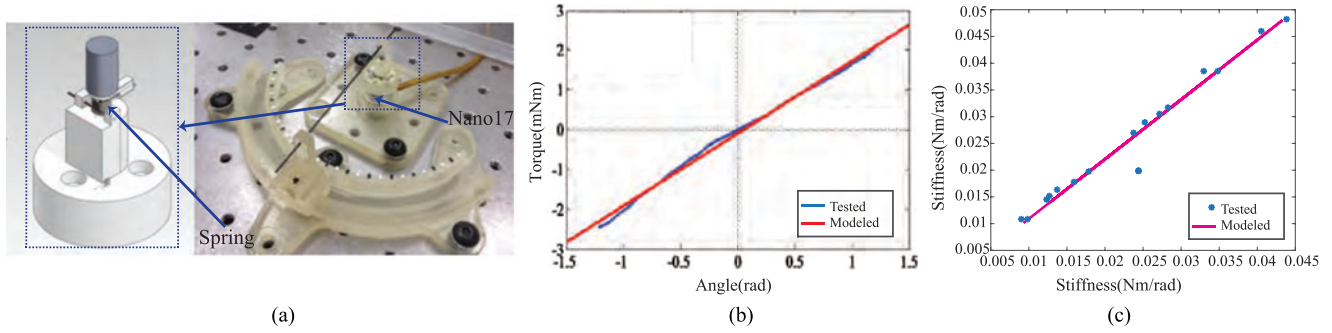
Fig. 6. (a) Experiment setup for testing springs. (b) Linearity test of spring. (c) Predicted spring stiffness (red line) versus the measured values (blue dots) for 16 springs.
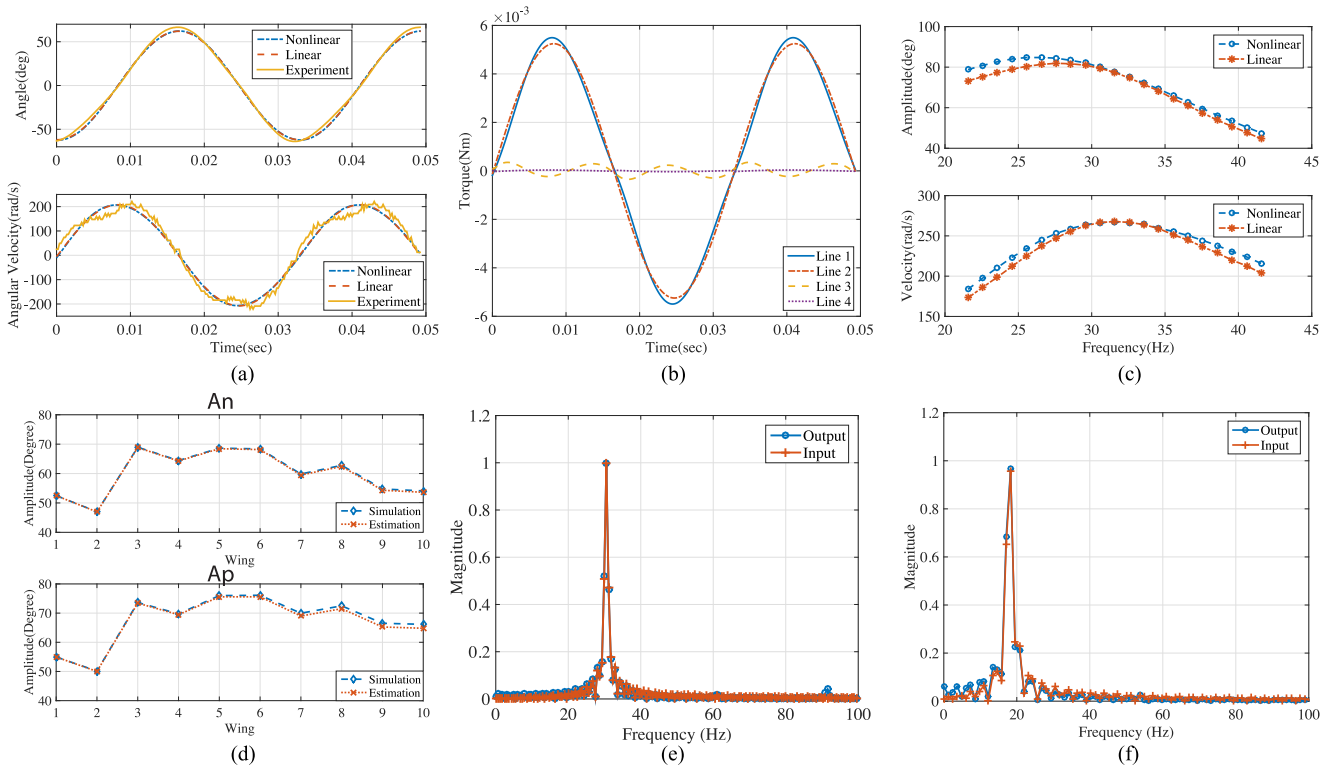

Fig. 7. (a) Nonlinear model simulation, linear model simulation, and experiment data. (b) Line 1: nonlinear damping torque, Line 2: linear damping torque, Line 3: nonlinear conservative torque, Line 4: linear conservative torque. (c) Linear model (39) only approximates nonlinear model well at natural frequency. (d) Predicted and simulated amplitudes at natural frequency and peak frequency. Single-sided amplitude spectrum of input voltage $u(t)$ and stroke angle $\phi(t)$ scaled to unity for better comparison: (e) is from experiment data at natural frequency; (f) is from simulation data at other frequency.

sinusoidal input at frequency different from natural frequency, around 0.6 times of natural frequency, was run with nonlinear model (11). It is shown that the output responses of the flapping motions to the sinusoidal input voltages were mostly sinusoidal, for both experiment and simulation, at and off natural frequency.

D. Frequency Sweep Test

To verify the proposed method, frequency responses for total ten wings were obtained. For frequency sweep test for each wing, the wing was driven at a sinusoidal input voltage $u = V_{\text{in}}\cos(\Omega t + \beta)$ with sufficient large amplitude V_{in}, while the frequency Ω varied from 20 to 45 Hz. Each test run over 40 s with a frequency step size of 1 Hz. Between frequency steps, the input voltage frequency was maintained for 5 s, which is much longer than the wingbeat period, so that the wing response had sufficient time to reach steady state. The forces were measured with the beam setup shown in Fig. 4, and the wing flapping angle was recorded with the motor encoder.

For data processing, during each step, the later 2 s of force measurements were averaged to get the average lift. Amplitudes of angle and the angular velocity of the stroke motion were extracted from the maximum values of the steady-state responses. The results for wing #1 to #10 are plotted to show the frequency
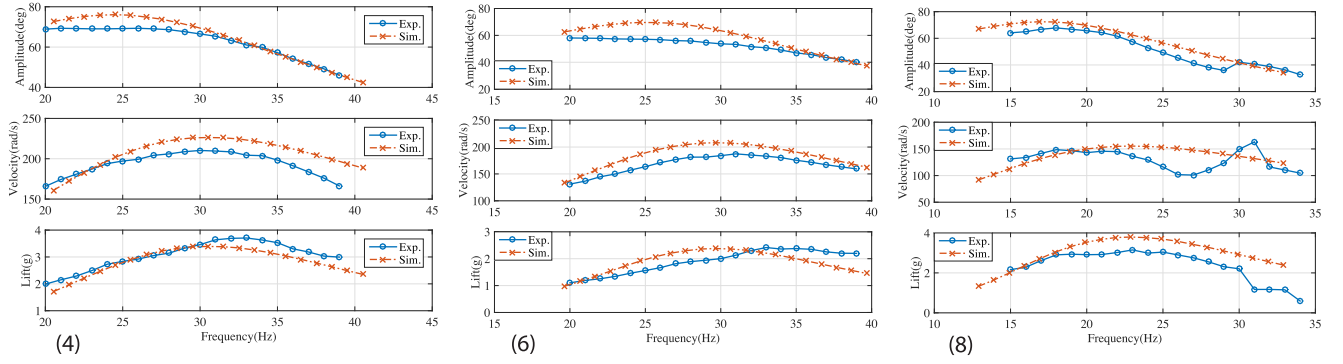
Fig. 8. Plots of frequency response for the frequency sweep experiments (blue) and simulations (red) (#4, #6, and #8 shown here as examples).
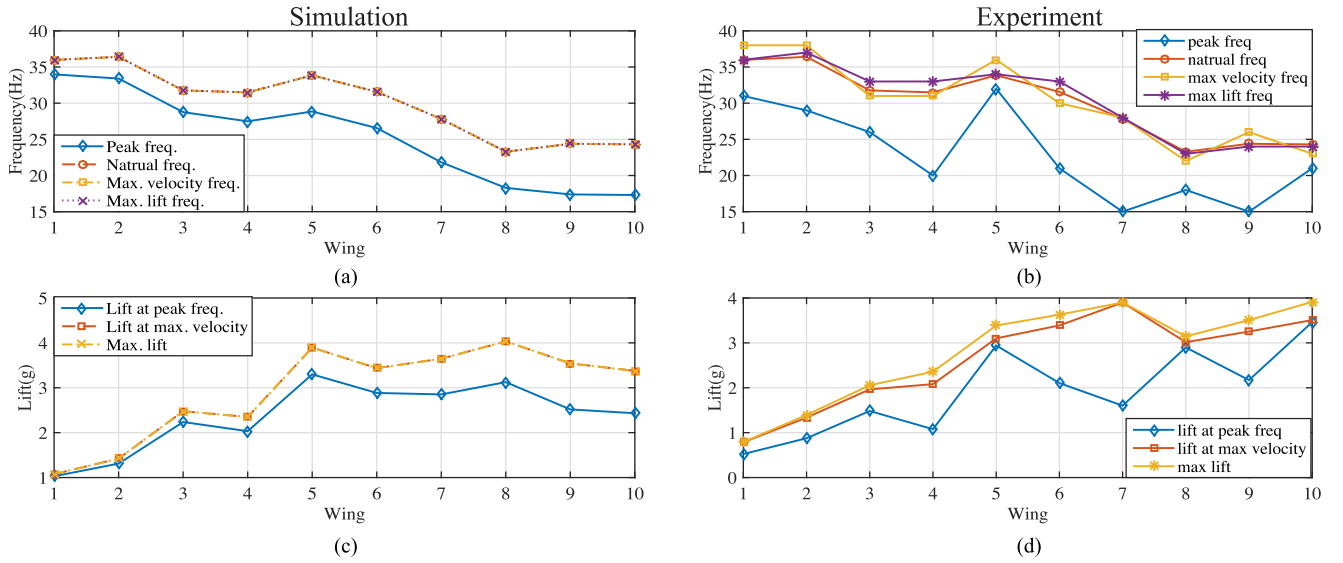

Fig. 9. Comparisons of peak frequencies, natural frequencies, maximum-velocity frequencies, and maximum-lift frequencies from (a) simulations and (c) experiments for ten wings. Comparisons of lifts at peak frequencies, lift at maximum-velocity frequencies, and maximum lift from (b) simulations and (d) experiments for ten wings.

response of the stroke amplitude, stroke angular velocity amplitude, and the mean lift force as functions of frequencies, as shown in Fig. 8, respectively.

As a comparison, numerical simulations with the nonlinear flapping wing dynamics (25) were run. Parameters for each simulation was based on the corresponding experiment. The frequency responses from experiments and simulations were plotted together with experiment results in red and simulation in blue, as shown in Fig. 8. Among all the wings, it is clear that the model (25) predicted the steady-state response and mean lift reasonably well over all tested wings and frequencies, as blue and red data points were relatively close. The discrepancies between the model and experiments are within reasonable levels, despite the quasi-steady model is inherently an approximation to the unsteady aerodynamics with possible 30% error comparing to experiments, as examined in [1].

E. Examination of Resonance

From frequency responses in Fig. 8, following key quantities were extracted: the peak frequency ω_p where stroke amplitude
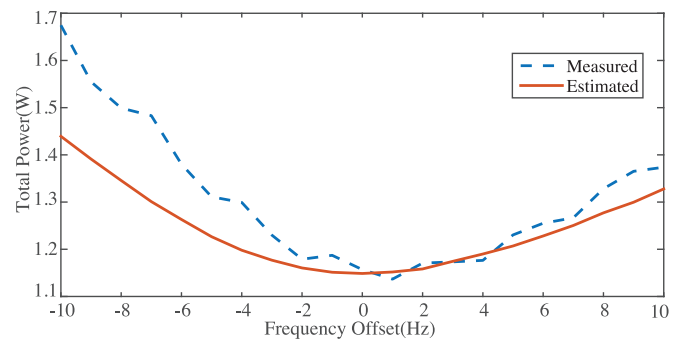

Fig. 10. Experiment shows the total power of the flapping wing system as a function of deviation from natural frequency for wing #6 as an example.

is maximum in frequency responses, denoted as peak freq. in the figure; the frequency that corresponds to maximum angular velocity in frequency responses, denoted as max.-velocity freq.; the frequency that gives the maximum lift in frequency responses, denoted as max. lift freq.; the lift at peak freq.; the lift at max. velocity; and the lift peak, denoted as max. lift. Along
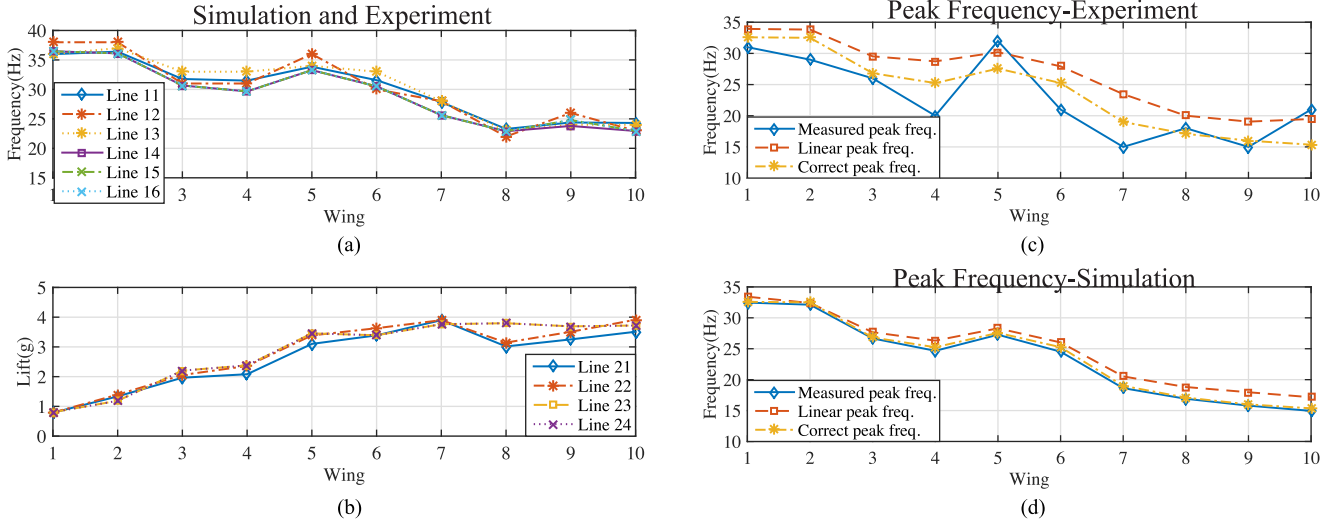
Fig. 11. For better comparisons between simulations and experiments, natural frequencies, maximum-velocity frequencies, and maximum-lift frequencies are plotted together in (a) to show their match, where Line 11 is natural frequencies from experiments, Line 12 is maximum-velocity frequencies from experiments, Line 13 is maximum-lift frequencies from experiments, Line 14 is natural frequencies from simulations, Line 15 is maximum-velocity frequencies from simulations, and Line 16 is maximum-lift frequencies from simulations; lifts at maximum-velocity frequencies and maximum lifts from simulations and experiments are plotted together in (b) to show their match, where Line 21 is lifts at maximum-velocity frequencies from experiments, Line 22 is maximum lift from experiments, Line 23 is lifts at maximum-velocity frequencies from simulations, and Line 24 is maximum lift from simulations. (c) Comparison of measured, estimated, and corrected peak frequencies from experiments for ten wings. (d) Comparison of measured, estimated, and corrected peak frequencies from simulations for ten wings. (Note: The line connecting data points in this plot are not for interpolation between wings.)

with the calculated natural frequency ω_n, above quantities for all ten wings were compiled in Fig. 9(c) and (d). Corresponding quantities extracted from simulations of the nonlinear model were compiled in Fig. 9(a) and (b). We have the following observations.

First, Fig. 9(a)–(d) confirmed that maximum lift and maximum angular velocity occur when driving the system at the natural frequency, not the peak frequency. In Fig. 11(a) and (b), for better comparisons between simulations and experiments, natural frequencies, maximum-velocity frequencies, maximum-lift frequencies, lifts at maximum-velocity frequencies, and maximum lifts were plotted together to show consistent matches.

Second, we validated the formula (41) for predicting peak frequency ω_p. In addition, we illustrated that the formula $\omega_p' = \sqrt{1 - 2\xi^2}\omega_n$ from traditional linear system theory is not valid for this system, compared to the proposed one (41). We denoted the peak frequencies from formula $\omega_p' = \sqrt{1 - 2\xi^2}\omega_n$ as linear peak freq. and ones from (41) as corrected peak freq. The measured and predicted ones were compared side by side in Fig. 11(c) for experiments and Fig. 11(d) for simulations. Predictions from formula (41) matched with better precision than formula $\omega_p' = \sqrt{1 - 2\xi^2}\omega_n$ for both experiments and simulations for all wings. This is due to the fact that the linear model (39) is only accurate around natural frequency ω_n, as the damping ratio ξ depends on the linear damping term, which, in turn, is a function of $A\Omega$. As ω_p is smaller than ω_n, the linear model is no more accurate, discrepancies between the measured ones from experiment and predicted ones based on the wrong formula were clearly shown in Fig 11(c) and (d).

Finally, to show that the maximum efficiency is achieved when the system is driven at the natural frequency, not the peak

frequency, experiments showed the total power measured with the DC power supply of the flapping wing system as a function of deviation from natural frequency, in Fig. 10 for wing #6, as an example. For other wings, the power plots are similar qualitatively.

F. Discussion

Figs. 9 and 11 showed that the wing #5 had largest discrepancies. We speculate that the discrepancies were due to the relatively long chord length of wing #5, which induced large chordwise flexing of the wing.

Fig. 9(a)–(d) shows that the general trend of the separations between natural frequency and peak frequency grew as the wing size increased and frequency decreased. This means that the above discussion will be more important for low-frequency flapping wings.

We here clarify the design goal for flapping resonance. Previous works such as [29] and [30] were driving the wing at damped natural frequency in the hope of getting optimal efficiency. We showed from theory and experiments that the best choice should be natural frequency for better efficiency. It is well known that sufficient large flapping amplitude ensures good passive rotation and thus good lift generation. Several previous works [6], [11], [16], [28] adopted maximizing the stroke amplitude as their design goal, even though the real design target should be to maximize the lift generation and optimize efficiency. Instead of driving the system at natural frequency, previous works commonly resorted to damped natural frequency or peak frequency to generate larger amplitudes. In this work, we showed that this is a suboptimal design decision. From the closed-form solution (38), we argue that this seeming tradeoff can be resolved

simply by increasing the input amplitude V_{in} or choosing actuator parameters to optimize K_u or $B_s 1$. From the analysis and experiments, we argue that the design goal for flapping resonance should be to maximize lift and efficiency by driving the wing at natural frequency, where the flapping velocity is also maximized. Increasing input voltage can ensure that the flapping amplitude is sufficiently large for good passive rotation.

We here reexam some of the possible misinterpretations of previous experiment results. Previous works such as [26], [28], and [31] confused natural frequency with peak frequency, using peak frequency from experiment frequency response to validate the value calculated from the equation of natural frequency. Here, we propose the correct experimental approach to validate that the natural frequency is, from frequency response, to find the frequency that maximizes flapping velocity, instead of flapping angle. In [14], the peak frequency was used as the indication of maximum lift and best efficiency, but later in the experiment frequency response, it was observed that the peak frequency actually appeared lower than the one under which maximum lift is produced (off-resonance maximum lift). In this study, we show that maximum lift is produced at natural frequency, which is typically higher than the peak frequency, thus explaining the observed discrepancy. Similar cases can also be seen in [28] and [31].

Last but not least, we propose the correct experimental approach to identify and validate the resonance of the system (natural frequency) is by conducting a frequency sweep, from the resulting frequency response, the frequency corresponding to the maximum value of the steady-state flapping velocity is the natural frequency of the system. Driving the system at this natural frequency, the maximum lift and maximum efficient will be achieved.

V. CONCLUSION AND FUTURE WORK

Mechanical resonance has been recognized as a key principle both by biologists and engineers for reducing the cost of driving high-frequency flapping wing motions. Elastic elements are typically incorporated for restoring the high inertial energy of oscillating wing. In this work, we analyzed dynamics of flapping wing as a nonlinear forced second-order resonant system, using both the nonlinear perturbation method and the linear approximation approach. We derived analytic formulas for steady-state flapping amplitude, energetics, and characteristic frequencies, including natural frequency, damped natural frequency, and peak frequency. The analysis revealed that both lift and efficiency are maximized by driving the wing at the natural frequency. Interestingly, the flapping velocity is maximized at the natural frequency as well, which can serve as a convenient experiment approach to identify the natural frequency and validate the resonance design. The modeling and analysis were validated with both simulations and experiments on ten different wings and a direct-motor-drive FWMAV. Furthermore, our analysis also explained some lingering questions on experiment results of previous works using the proposed method.

Future work includes using this study as a systematic resonance design tool to guide the initial design decisions for later fine-tuning and iteration of the system design parameters. The results will be incorporated as a part of a formulation for whole vehicle design optimization, as the proposed analytic formulas give insights on how system parameters and resonance affect force generation and energetics. Current study can clarify the confusion about resonance for designing and prototyping of FWMAV, as well as help biologists study resonance of insects' flapping wing system.

REFERENCES

[1] M. H. Dickinson, F.-O. Lehmann, and S. P. Sane, "Wing rotation and the aerodynamic basis of insect flight," *Science*, vol. 284, no. 5422, pp. 1954–1960, 1999.

[2] S. N. Fry, R. Sayaman, and M. H. Dickinson, "The aerodynamics of free-flight maneuvers in drosophila," *Science*, vol. 300, no. 5618, pp. 495–498, 2003.

[3] A. J. Bergou, L. Ristroph, J. Guckenheimer, I. Cohen, and Z. J. Wang, "Fruit flies modulate passive wing pitching to generate in-flight turns," *Phys. Rev. Lett.*, vol. 104, no. 14, 2010, Art. no. 148101.

[4] T. Weis-Fogh, "Dimensional analysis of hovering flight," in *Scale Effects in Animal Locomotion*. London, U.K.: Academic, 1977, pp. 405–420.

[5] X. Deng, L. Schenato, W. C. Wu, and S. S. Sastry, "Flapping flight for biomimetic robotic insects: Part I-system modeling," *IEEE Trans. Robot.*, vol. 22, no. 4, pp. 776–788, Aug. 2006.

[6] R. J. Wood, "The first takeoff of a biologically inspired at-scale robotic insect," *IEEE Trans. Robot.*, vol. 24, no. 2, pp. 341–347, Apr. 2008.

[7] V. Arabagi, L. Hines, and M. Sitti, "Design and manufacturing of a controllable miniature flapping wing robotic platform," *Int. J. Robot. Res.*, vol. 31, pp. 785–800, 2012.

[8] M. Keennon, K. Klingebiel, H. Won, and A. Andriukov, "Development of the nano hummingbird: A tailless flapping wing micro air vehicle," in *Proc. 50th AIAA Aerosp. Sci. Meeting Including New Horizons Forum Aerosp. Expo., Aerosp. Sci. Meetings*, 2012.

[9] C. Richter and H. Lipson, "Untethered hovering flapping flight of a 3D-printed mechanical insect," *Artif. Life*, vol. 17, no. 2, pp. 73–86, 2011.

[10] G. De Croon, K. De Clercq, R. Ruijsink, B. Remes, and C. De Wagter, "Design, aerodynamics, and vision-based control of the delfly," *Int. J. Micro Air Veh.*, vol. 1, no. 2, pp. 71–97, 2009.

[11] J. Zhang, B. Cheng, J. A. Roll, X. Deng, and B. Yao, "Direct drive of flapping wings under resonance with instantaneous wing trajectory control," in *Proc. IEEE Int. Conf. Robot. Autom.*, May 2013, pp. 4029–4034.

[12] J. Zhang, B. Cheng, B. Yao, and X. Deng, "Adaptive robust wing trajectory control and force generation of flapping wing MAV," in *Proc. IEEE Int. Conf Robot. Autom.*, 2015, pp. 5852–5857.

[13] Q. V. Nguyen, Q. T. Truong, H. C. Park, N. S. Goo, and D. Byun, "A motor-driven flapping-wing system mimicking beetle flight," in *Proc. IEEE Int. Conf. Robot. Biomimetics*, 2009, pp. 1087–1092.

[14] L. Hines, D. Campolo, and M. Sitti, "Liftoff of a motor-driven, flapping-wing microaerial vehicle capable of resonance," *IEEE Trans. Robot.*, vol. 30, no. 1, pp. 220–232, Feb. 2014.

[15] G.-K. Lau, Y.-W. Chin, J.-W. Goh, and R. J. Wood, "Dipteran-insect-inspired thoracic mechanism with nonlinear stiffness to save inertial power of flapping-wing flight," *IEEE Trans. Robot.*, vol. 30, no. 5, pp. 1187–1197, Oct. 2014.

[16] J. A. Roll, B. Cheng, and X. Deng, "Design, fabrication, and experiments of an electromagnetic actuator for flapping wing micro air vehicles," in *Proc. IEEE Int. Conf. Robot. Autom.*, May 2013, pp. 809–815.

[17] C. H. Greenewalt, "The wings of insects and birds as mechanical oscillators," in *Proc. Amer. Philos. Soc.*, pp. 605–611, 1960.

[18] R. Dudley, *The Biomechanics of Insect Flight: Form, Function, Evolution.* Princeton, NJ, USA: Princeton Univ. Press, 2002.

[19] D. Floreano and R. J. Wood, "Science, technology and the future of small autonomous drones," *Nature*, vol. 521, no. 7553, pp. 460–466, 2015.

[20] K. Y. Ma, P. Chirarattananon, S. B. Fuller, and R. J. Wood, "Controlled flight of a biologically inspired, insect-scale robot," *Science*, vol. 340, no. 6132, pp. 603–607, 2013.

[21] T. Tantanawat and S. Kota, "Design of compliant mechanisms for minimizing input power in dynamic applications," *J. Mech. Des.*, vol. 129, no. 10, pp. 1064–1075, 2007.

[22] R. Madangopal, Z. A. Khan, and S. K. Agrawal, "Biologically inspired design of small flapping wing air vehicles using four-bar mechanisms and quasi-steady aerodynamics," *J. Mech. Des.*, vol. 127, no. 4, pp. 809–816, 2005.

[23] Z. A. Khan and S. K. Agrawal, "Design and optimization of a biologically inspired flapping mechanism for flapping wing micro air vehicles," in *Proc. IEEE Int. Conf. Robot. Autom.*, 2007, pp. 373–378.

[24] S. S. Baek, K. Y. Ma, and R. S. Fearing, "Efficient resonant drive of flapping-wing robots," in *Proc. IEEE/RSJ Int. Conf. Intell. Robots Syst.*, 2009, pp. 2854–2860.

[25] R. Madangopal, Z. A. Khan, and S. K. Agrawal, "Energetics-based design of small flapping-wing micro air vehicles," *IEEE/ASME Trans. Mechatronics*, vol. 11, no. 4, pp. 433–438, Aug. 2006.

[26] M. Azhar, D. Campolo, G.-K. Lau, L. Hines, and M. Sitti, "Flapping wings via direct-driving by dc motors," in *Proc. IEEE Int. Conf. Robot. Autom.*, 2013, pp. 1397–1402.

[27] B. M. Finio, N. O. Pérez-Arancibia, and R. J. Wood, "System identification and linear time-invariant modeling of an insect-sized flapping-wing micro air vehicle," in *Proc. IEEE/RSJ Int. Conf. Intell. Robots Syst.*, 2011, pp. 1107–1114.

[28] M. Sitti, "Piezoelectrically actuated four-bar mechanism with two flexible links for micromechanical flying insect thorax," *IEEE/ASME Trans. Mechatronics*, vol. 8, no. 1, pp. 26–36, Mar. 2003.

[29] K. Y. Ma, S. M. Felton, and R. J. Wood, "Design, fabrication, and modeling of the split actuator microrobotic bee," in *Proc. IEEE/RSJ Int. Conf. Intell. Robots Syst.*, 2012, pp. 1133–1140.

[30] D. Campolo, M. Azhar, G.-K. Lau, and M. Sitti, "Can DC motors directly drive flapping wings at high frequency and large wing strokes?" *IEEE/ASME Trans. Mechatronics*, vol. 19, no. 1, pp. 109–120, Feb. 2014.

[31] R. J. Wood, "Design, fabrication, and analysis of a 3DOF, 3cm flapping-wing MAV," in *Proc. IEEE/RSJ Int. Conf. Intell. Robots Syst.*, 2007, pp. 1576–1581.

[32] C. Ellington, "The aerodynamics of hovering insect flight. II. Morphological parameters," *Philos. Trans. Royal Soc. London B, Biol. Sci.*, vol. 305, no. 1122, pp. 1–15, 1984.

[33] A. J. Bergou, S. Xu, and Z. Wang, "Passive wing pitch reversal in insect flight," *J. Fluid Mech.*, vol. 591, pp. 321–337, 2007.

[34] A. L. Desbiens, Y. Chen, and R. J. Wood, "A wing characterization method for flapping-wing robotic insects," in *Proc. IEEE/RSJ Int. Conf. Intell. Robots Syst.*, 2013, pp. 1367–1373.

[35] J. Zhang, B. Cheng, and X. Deng, "Instantaneous wing kinematics tracking and force control of a high-frequency flapping wing insect MAV," *J. Micro-Bio Robot.*, pp. 1–18, 2016.

[36] J. Whitney and R. Wood, "Conceptual design of flapping-wing micro air vehicles," *Bioinspiration Biomimetics*, vol. 7, no. 3, 2012, Art. no. 036001.

[37] A. H. Nayfeh and D. T. Mook, *Nonlinear Oscillations*. Hoboken, NJ, USA: Wiley, 2008.

[38] B. Cheng, J. A. Roll, and X. Deng, "Modeling and optimization of an electromagnetic actuator for flapping wing micro air vehicle," in *Proc. IEEE Int. Conf. Robot. Autom.*, May 2013, pp. 4035–4041.
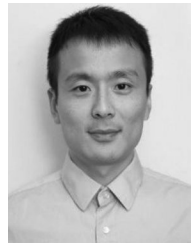
Jian Zhang received the B.S. degree in mechatronics from Zhejiang University, Hangzhou, China, in 2010 and the Ph.D. degree in mechanical engineering from Purdue University, West Lafayette, IN, USA, in 2015.

Xinyan Deng (M'04) received the B.S. degree in automation from Tianjin University, Tianjin, China, in 1995 and the Ph.D. degree in mechanical engineering from University of California, Berkeley, CA, USA, in 2004.

She was an Assistant Professor with the Department of Mechanical Engineering, University of Delaware, Newark, DE, USA, from 2004 to 2009. She is currently an Associate Professor with the School of Mechanical Engineering, Purdue University, West Lafayette, IN, USA. Her research interests include bioinspired robots, micro air vehicles, and underwater vehicles.